S700 high-strength cold-formed steel built-up I-section stub columns: Testing, numerical modelling and design

Chicheng Ma [a, b], Ke Jiang [c], Andi Su [a, b, *], Ou Zhao [d], Leroy Gardner [e]

[a] Key Lab of Structures Dynamic Behavior and Control of the Ministry of Education, Harbin Institute of Technology, Harbin, 150090, China

[b] Key Lab of Smart Prevention and Mitigation of Civil Engineering Disasters of the Ministry of Industry and Information Technology, Harbin Institute of Technology, Harbin, 150090, China

[c] Department of Civil and Natural Resources Engineering, University of Canterbury, Christchurch, New Zealand

[d] School of Civil and Environmental Engineering, Nanyang Technological University, Singapore

[e] Department of Civil and Environmental Engineering, Imperial College London, UK

* Corresponding author, Email: a.su@hit.edu.cn

Abstract

This paper presents experiments and numerical simulations on S700 high-strength cold-formed steel (CFS) built-up I-section stub columns to investigate their cross-sectional behaviour and resistance. Each built-up I-section comprised two identical press-braked channel sections assembled back-to-back using G12-24TPI screws. The experimental programme was firstly conducted, including tensile coupon tests, measurements of initial local geometric imperfections and twelve stub column compression tests. Local buckling was identified for all

the specimens upon testing, but with no failure found in the screws or the adjacent material. The numerical programme was then performed, where stub column finite element models were established and validated against the experimental results and parametric studies were conducted to generate further numerical data. The generated results were used to assess the applicability of the current European and American design guidelines for CFS structures to S700 high-strength CFS built-up I-section stub columns. Both the effective width and direct strength methods were considered and each was shown generally to yield consistent and accurate resistance predictions, though with some scope for improvement. Modified design provisions based on the Direct Strength Method were thus proposed for S700 high-strength CFS built-up I-section stub columns and shown to result in improved design accuracy.

Keywords

S700 high-strength cold-formed steel; built-up I-section stub columns; connection elements; experiments; finite element modelling; structural design.

1. Introduction

In cold-formed steel (CFS) construction, built-up sections, which are composed of several component sections fastened together with screws or welded, are gaining increasing use due to the flexible cross-sectional shapes and convenient fabrication process. Compared with singly, monosymmetric sections, doubly-symmetric built-up I-section has high load-bearing capacity

and, with the centroid and shear centre being coincident, are less prone to torsional effects [1–3]. For conventional structural elements in high or ultra-high strength steel, the behaviour and design of welded I-section members have been systematically studied by Su et al. [4–10], Sun et al. [11, 12], Shi et al. [13, 14] and Yun et al. [15]. However, research into high-strength CFS built-up I-section members is relatively limited, as summarised hereinafter. Abbasi et al. [16] examined the local buckling behaviour and cross-sectional resistance of G450 high-strength CFS built-up I- and multi-limb section columns under pure compression. A series of compression tests, numerical simulations and improved design equations on G500 and G550 high-strength CFS built-up I-section columns with stiffened webs and flanges were reported by Zhang and Young [17, 18] and Li and Young [19]. Roy et al. [20–22], Li et al. [23] and Ting et al. [24] experimentally and numerically investigated the effects of thickness, screw spacing and installation errors on the buckling behaviour and load-carrying capacity of G550 high-strength CFS built-up I-section columns, composed of lipped and unlipped channel sections. Wang and Young [25–27], Phan and Rasmussen [1], and Roy et al. [28, 29] studied the bending behaviour and resistance of G450 and G550 high-strength CFS built-up I-section beams and proposed improved design rules. The aforementioned studies focussed on CFS built-up I-section members with a maximum nominal yield strength of 550 MPa. The use of high-strength steel with nominal yield strength of between 690MPa and 960MPa has been increasingly prevalent in engineering practices due to its superior strength-to-weight ratio compared to normal strength steel, allowing structural members to be designed with smaller sizes and simpler configurations. However, owing to the lack of accurate design rules, the application of high-strength CFS built-

up section members is hindered, which has prompted research into S700 high-strength CFS built-up I-section members herein.

The focus of the present paper is on the cross-sectional buckling behaviour and resistance of S700 high-strength CFS built-up I-section stub columns under compression. An experimental programme, including tensile coupon tests, initial local geometric imperfection measurements and twelve compression tests on stub columns, was firstly carried out. Then, parallel finite element (FE) analyses were conducted, where FE models were initially developed to replicate the test results and extensive parametric studies were subsequently performed to generate further FE data over a wide range of cross-sectional dimensions. Based on the test results and FE data, the applicability of the Effective Width Method (EWM) in EN 1993-1-3 [30] and AISI S100 [31] and the Direct Strength Method (DSM) in AISI S100 [31] was evaluated. Finally, a modified DSM design expression was proposed and its reliability was verified.

2. Experimental programme

2.1. Test specimens

Twelve S700 high-strength CFS built-up I-section stub column specimens were tested in the experimental programme, where each specimen consisted of two identical unlipped channel section members arranged back-to-back and connected by G12-24TPI screws [32] – see Fig. 1,

with the geometric dimensions and material reported in Table 1. Owing to the high toughness of S700 high-strength steel, gauge holes were pre-drilled in the S700 high-strength CFS sheet at the specified screw positions. Seven cross-sectional dimensions of the built-up I-sections were employed, including 60 × 40 × 2.7, 80 × 50 × 2.7, 90 × 70 × 2.7, 100 × 100 × 2.7, 120 × 90 × 2.7, 140 × 120 × 2.7 and 160 × 100 × 2.7 (outer cross-sectional height h × outer cross-sectional width b × nominal thickness t). All the channel sections were press-braked from S700 high-strength CFS sheets with a nominal thickness of 2.7 mm. The inner corner radius was equal to 3 mm, which is in compliance with the relevant requirements of AISI S100 [31]. Fig. 1 shows the screw arrangement, where the screws were located at the quarter-heights of the built-up I-sections. The screw spacings along the column length direction are shown in Fig. 2, where a is the evenly distributed screw spacing and s is the end spacing between the centre of the outermost screw and the end of the stub column specimen. The evenly distributed screw spacings of 50 mm comfortably satisfied the codified limit of 315 mm obtained from the relevant requirements in AISI S100 [31], as shown in Eq. (1), where $(kL/i)_o$ is the slenderness ratio about the minor principal axis and i_s is the minimum radius of gyration of the component channel section. The nominal length of each stub column specimen was selected to be three times the average of the nominal outer height and width of the component channel sections. Prior to testing, the geometric dimensions of all specimens were measured and are reported in Table 2. The specimen ID begins with the letter 'I' (signifying a built-up I-section) and is followed by the nominal dimensions of the specimens (h × b), with a symbol '*' referring to a repeated test.

$$a \le \frac{i_s}{2}\left(\frac{kL}{i}\right)_o \tag{1}$$

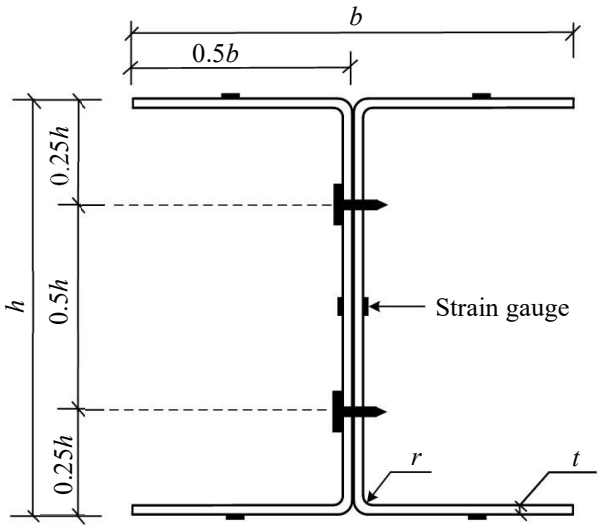


Fig. 1. Notation of built-up I-sections and locations of strain gauges.

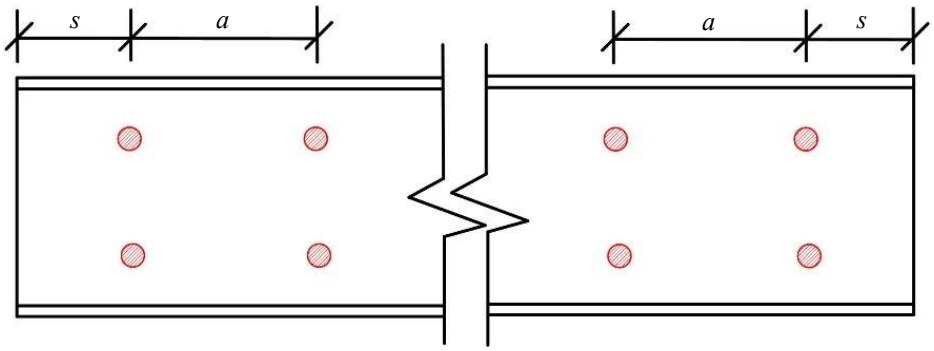


Fig. 2. Longitudinal arrangement of fasteners.

Table 1

Geometric dimensions and material grade of employed G12-24TPI screws.

Screw	Nominal diameter (mm)	Effective length (mm)	Threads per inch (TPI)	Material grade
G12-24TPI	5.5	16.0	24	EN 1.4301

Table 2

Measured geometric dimensions and initial local geometric imperfections of S700 high-strength CFS built-up I-section stub column specimens.

Specimen ID	a (mm)	s (mm)	h (mm)	b (mm)	t (mm)	L (mm)	r (mm)	ω_l (mm)	No. of rows of screws
I-60×40	50	25	59.2	37.2	2.7	150.1	3.0	0.23	3
I-80×50		20	80.1	47.3	2.7	190.2	3.0	0.28	4
I-90×70		20	89.4	67.6	2.8	240.2	3.0	0.25	5
I-90×70*		20	89.8	67.9	2.8	239.8	3.0	0.23	5
I-100×100		25	99.5	97.5	2.7	300.1	3.0	0.24	6
I-100×100*		25	99.7	97.3	2.7	300.0	3.0	0.30	6
I-120×90		5	119.6	87.4	2.7	309.8	3.0	0.23	6
I-120×90*		5	119.3	87.5	2.7	310.3	3.0	0.30	6
I-140×120		20	139.2	117.6	2.7	390.1	3.0	0.27	8
I-140×120*		20	139.7	116.9	2.7	390.0	3.0	0.33	8
I-160×100		20	159.1	97.5	2.8	390.0	3.0	0.32	8
I-160×100*		20	159.3	96.7	2.7	390.5	3.0	0.22	8

2.2. Material testing

The key mechanical properties and stress–strain curves of the S700 high-strength CFS material were obtained through the tensile coupon tests. Both flat and corner coupons were cut from the corresponding regions of channel sections along the longitudinal direction, with the dimensions in line with the relevant requirements of EN ISO 6892-1 [33] and detailed locations shown in Fig. 3. The flat coupons were 12.5 mm in width with a parallel length of 75 mm, while the corner coupons were 6 mm in width with a parallel length of 75 mm. The test setup is depicted in Fig. 4. Extensometers with gauge lengths of 50 mm and 100 mm were respectively attached to the parallel portion of the corner and flat coupons to measure the longitudinal elongations, while two strain gauges (one on each side) were mounted at the mid-height of the flat and corner coupons to monitor the longitudinal tensile strains. Referring to EN ISO 6892-1 [33], the

loading rates were chosen as 0.2 mm/min before the yield strength and 0.8 mm/min beyond yielding, with a moderate ramp at the transition point to prevent an abrupt rate change. Fig. 5 illustrates the measured static engineering stress–strain curves. Compared with the flat coupons, the corner coupons exhibited higher yield and ultimate stresses and lower ductility due to the press-braking process. The key measured material properties are presented in Table 3, where E is the elastic modulus, f_y and f_u are the yield and ultimate stresses, respectively, and ε_f is the fracture strain.

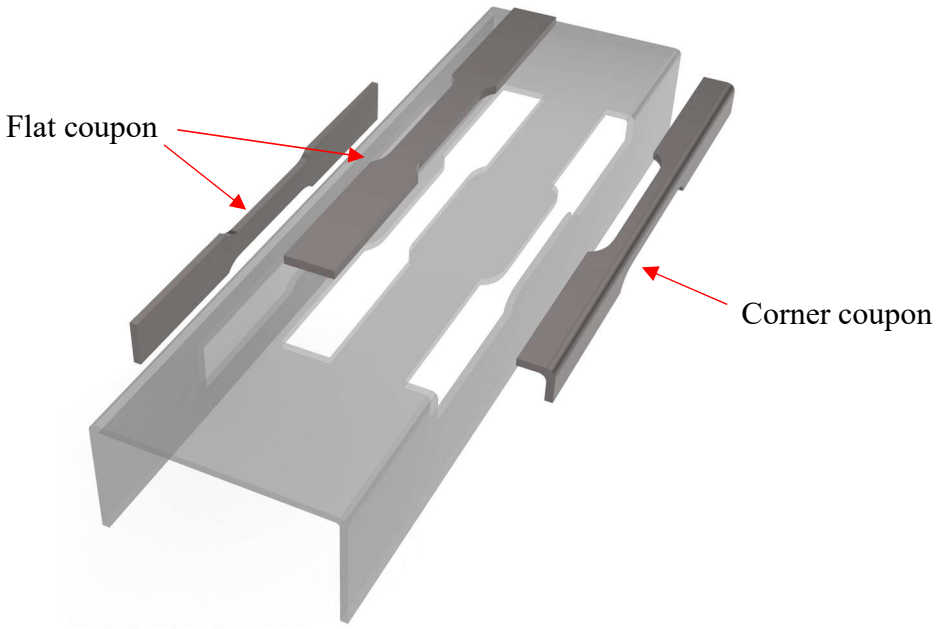


Fig. 3. Locations of coupons.

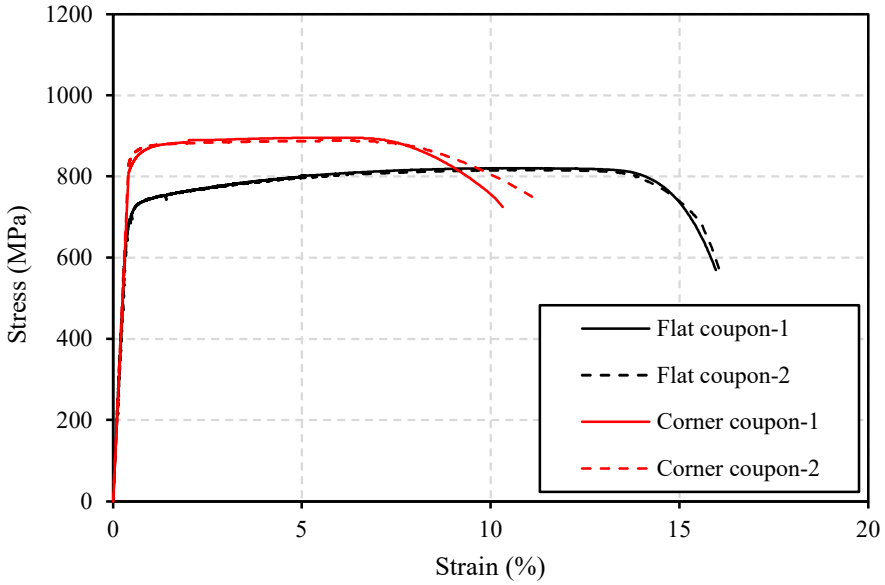


(a) Flat coupon (b) Corner coupon

Fig. 4. Tensile coupon test setup.

147

148



149

150 **Fig. 5.** Measured stress–strain curves.

151

152

153 **Table 3**

154 Measured material properties of tested CFS.

	E (GPa)	f_y (MPa)	f_u (MPa)	ε_f (%)
Flat coupon-1	192.50	726.17	816.08	17.90
Flat coupon-2	207.93	729.09	820.03	17.43
Corner coupon-1	197.04	863.66	894.97	10.32
Corner coupon-2	202.66	865.38	890.52	11.13

155

2.3. Measurements of initial imperfections

Initial local geometric imperfections can critically affect the cross-sectional buckling behaviour and resistance of thin-walled structural members [25–27, 34, 35]. Prior to testing, the initial local geometric imperfections of all stub column specimens were thus measured. The measurement setup is displayed in Fig. 6, by means of which, the following measurement procedure was followed: (i) the specimen was positioned on a flat workbench; (ii) a laser distance measurer moved transversely across one face of the cross-section; (iii) the specimen was rotated to measure all three faces of the cross-section; (iv) the above steps were repeated to measure the different cross-sections along the specimen length. The deviations of the measured data from the linear regression line fitted to the measured data were defined as the initial local geometric imperfections, with the largest deviation defined as the initial local geometric imperfection magnitude of the specimen ω_l, as reported in Table 2. Fig. 7 shows the distribution of the measured initial local geometric imperfections for the typical specimen I-160×100.

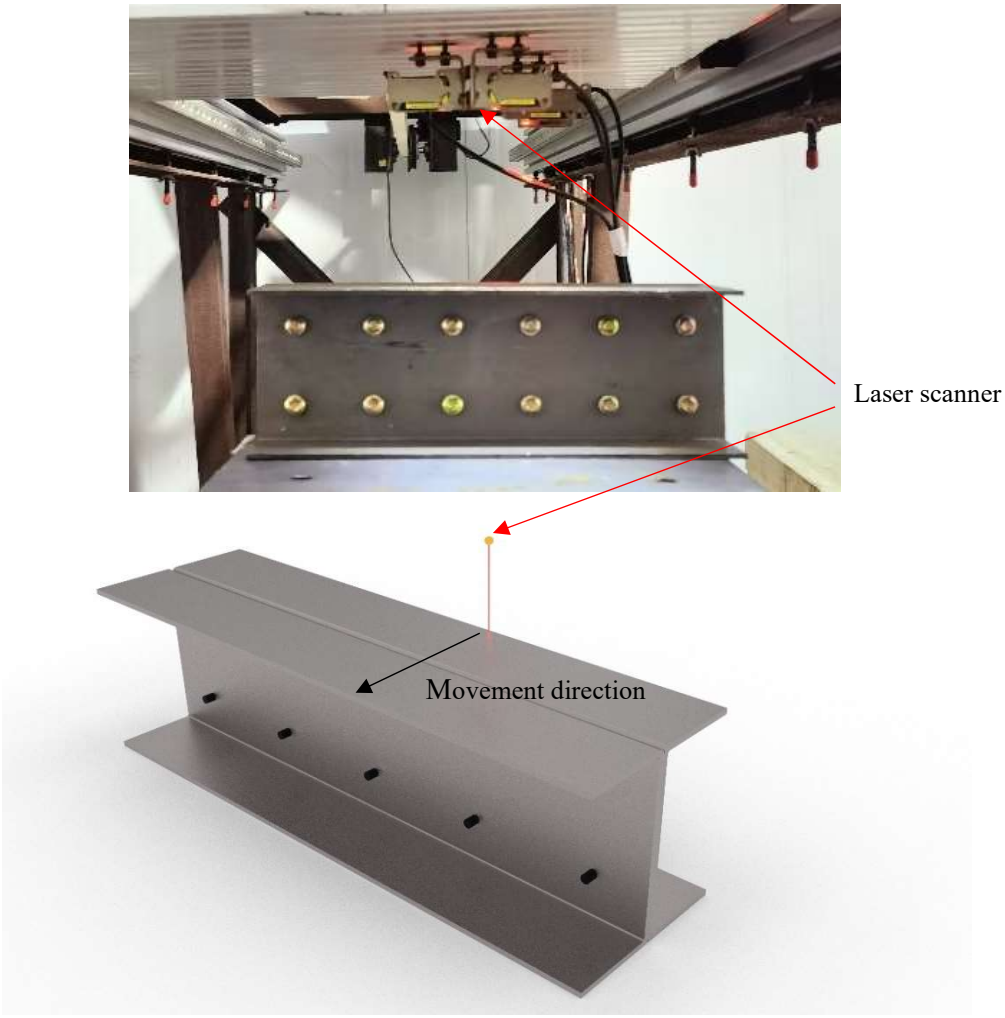


Fig. 6. Measurement setup for initial local geometric imperfections.

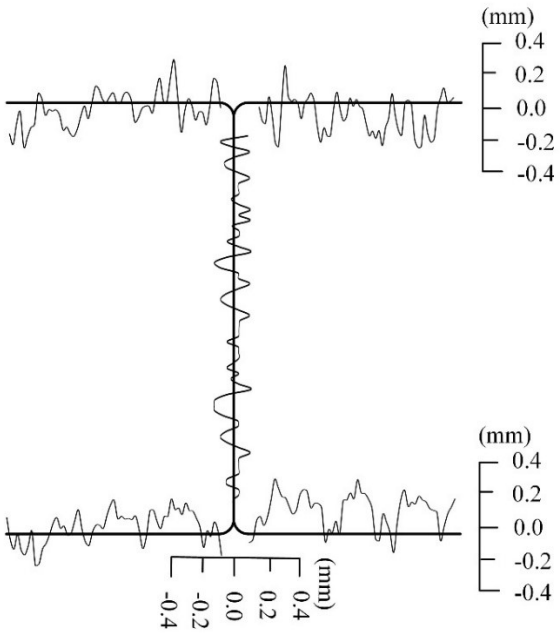
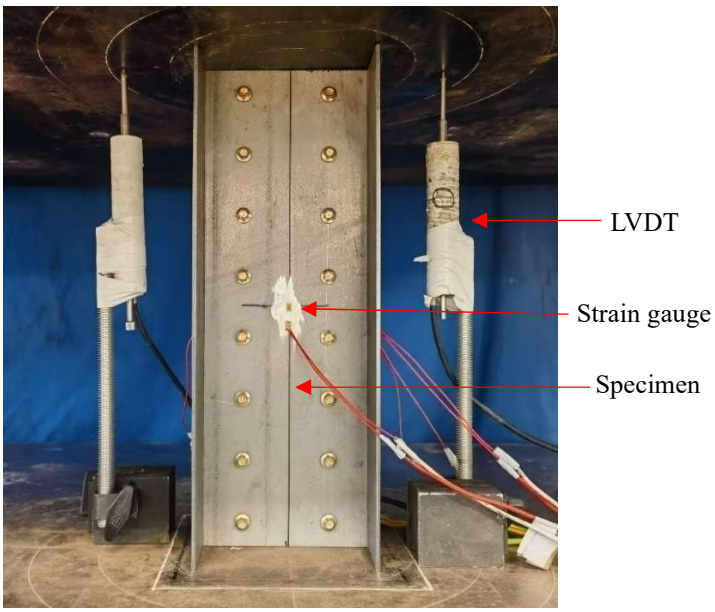


Fig. 7. Measured initial local geometric imperfection distribution of specimen I-160×100.

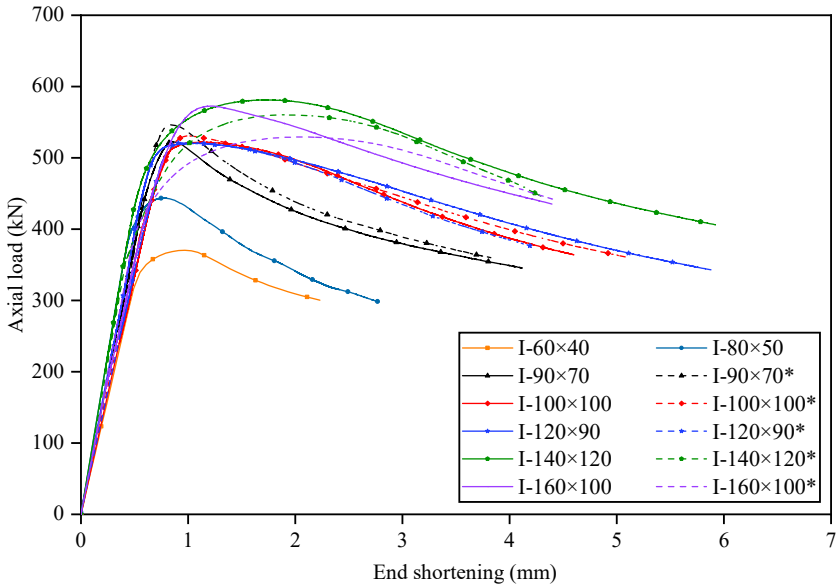
2.4. Stub column tests

Twelve fixed-ended S700 high-strength CFS built-up I-section stub column specimens were tested under compression to examine their cross-sectional resistances and local buckling behaviour. A displacement controlled hydraulic testing machine was adopted to apply axial compression loads at a constant rate of 0.1 mm/min. As shown in Fig. 8, a pair of LVDTs were vertically installed to obtain the end shortening and six strain gauges were attached at the mid-height of each specimen to record the longitudinal strains, with the detailed positions displayed in Fig. 1. The readings from the LVDTs consist of both the deformations of the specimens and the end platens of the testing machine. Hence, the end shortening readings were corrected [36] by using the strain gauge data to eliminate the end platen deformations from the LVDT measurements. Fig. 9 shows the corrected axial load–end shortening curves of all specimens, while Table 4 reports the key experimental results, including the failure load P_u and the end shortening at the failure load δ_u. Fig. 10 displays the failure modes of all tested S700 high-strength CFS built-up I-section stub column specimens, with no failure found in the self-tapping screws.



194
195 **Fig. 8.** Stub column test setup.

196



197
198 **Fig. 9.** Axial load–end shortening curves of S700 high-strength CFS built-up I-section stub column specimens.

199

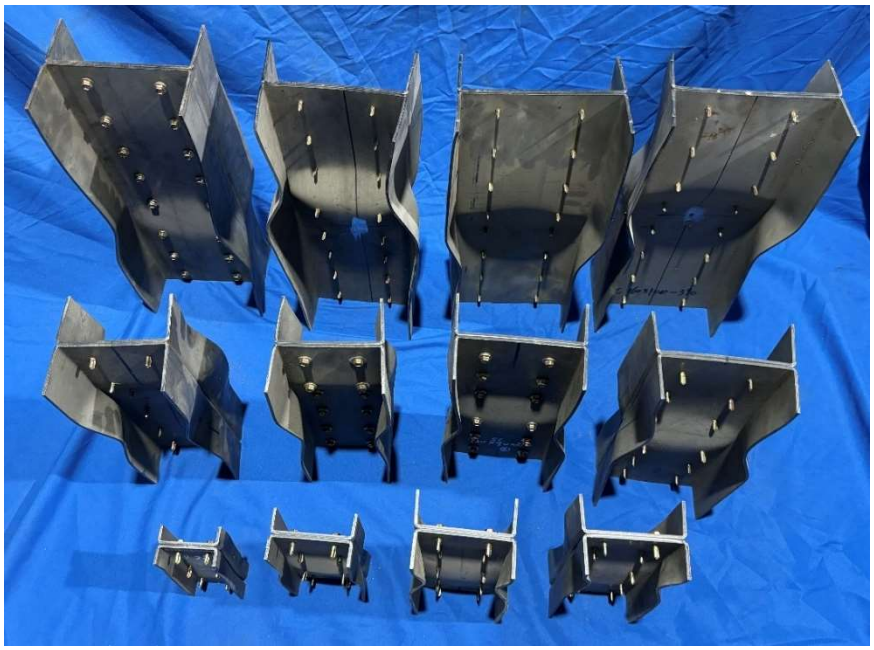


Fig. 10 Local buckling of S700 high-strength CFS built-up I-section stub column specimens.

Table 4

Summary of stub column test results.

Specimen ID	P_u (kN)	δ_u (mm)
I-60×40	370.4	0.98
I-80×50	443.6	0.80
I-90×70	528.4	0.87
I-90×70*	546.5	0.84
I-100×100	521.9	1.00
I-100×100*	533.2	0.99
I-120×90	520.3	1.05
I-120×90*	520.7	1.01
I-140×120	582.0	1.68
I-140×120*	560.3	1.82
I-160×100	576.1	1.05
I-160×100*	529.3	1.93

3. Numerical modelling

3.1. General

Numerical modelling was conducted by means of the finite element (FE) software ABAQUS [37]. FE models of S700 high-strength CFS built-up I-section stub columns were developed and validated against the experimental results, and then applied to perform parametric studies to generate further numerical data over a wide range of cross-sectional dimensions.

3.2. Development of FE models

3.2.1. Geometric and material modelling

All S700 high-strength CFS built-up I-section stub column FE models were established in accordance with the measured geometric dimensions in the validation study and the nominal dimensions in the parametric study. The shell element S4R [37], which has been effectively utilised in previous FE modelling of both plain [38, 39] and built-up [19, 40] section members, was adopted herein. Aiming to determine appropriate element sizes for efficient and accurate FE analyses, a mesh sensitivity study was carried out, with detailed results reported in Table 5, following which element sizes of $t \times t$ and $0.5t \times 0.5t$ for the flat and corner parts of the channel section members, respectively, were selected. Regarding the material modelling, Eqs. (2) and

(3) were used to convert the averaged engineering (measured) stress–strain curves into true stress–strain curves, where σ_{true} and ε_{ln}^{pl} are respectively the true stress and plastic strain, and σ_{nom} and ε_{nom} are respectively the engineering stress and strain; the resulting curves, represented by a series of discrete points, were then applied to the corresponding regions of stub column FE models. Residual stresses were not explicitly measured or modelled herein, since (i) the bending residual stresses inherently feature in the measured stress–strain curves [41, 42], (ii) the magnitudes of the membrane residual stresses in press-braked steel members are negligible [43, 44], and (iii) the effect of residual stresses on structural performance is less significant in high-strength steel sections [45].

$$\sigma_{true} = \sigma_{nom}(1+\varepsilon_{nom}) \tag{2}$$

$$\varepsilon_{ln}^{pl} = \ln(1+\varepsilon_{nom}) - \frac{\sigma_{nom}}{E} \tag{3}$$

Table 5

Comparisons of test failure loads with numerical failure loads for various element sizes.

		FE P_u/Test P_u		
Specimen ID	Flat region:	$2t \times 2t$	$t \times t$	$0.5t \times 0.5t$
	Corner region:	$t \times t$	$0.5t \times 0.5t$	$0.25t \times 0.25t$
I-60×40		1.10	1.09	1.07
I-80×50		1.05	1.03	1.01
I-90×70		1.05	1.00	0.99
I-90×70*		1.02	0.98	0.99
I-100×100		1.04	1.01	1.01
I-100×100*		1.03	1.00	1.00
I-120×90		1.04	1.00	1.00
I-120×90*		1.06	0.99	0.99
I-140×120		1.05	0.99	0.98
I-140×120*		1.04	1.00	1.00
I-160×100		1.02	0.97	0.99
I-160×100*		1.05	1.01	1.00
Mean		1.05	1.01	1.00
COV		0.02	0.03	0.02

241 *3.2.2. Contacts and boundary conditions*

242

243 The developed built-up section stub column FE model is shown in Fig. 11. The interaction
244 between the webs of the component channel section members was implemented as 'surface-to-
245 surface' contact, with 'hard' contact defined in the normal direction and 'frictionless' contact
246 adopted in the tangential direction. In order to simulate the fixed-ended boundary conditions
247 and prevent global buckling to ensure occurrence of local buckling, both end sections of the
248 stub column FE models were coupled to two concentric reference points, with one reference
249 point fully restrained and the other restrained against all degrees of freedom except longitudinal
250 translation. Three approaches were considered for modelling the screws – 'Actual screws',
251 'Coupling DOFs' and 'Fasteners'. The 'Actual screws' approach utilised solid C3D8R elements
252 [37] to model the actual screws and 'tie' constraints to secure each screw to the corresponding
253 screw holes. This approach has been successfully used in previous numerical simulations of
254 built-up section members [17, 19, 25, 46], but can suffer from extended computational times
255 and convergence issues. To address these problems, two simplified approaches are introduced
256 as follows. The 'Coupling DOFs' approach, which has been adopted in previous research into
257 built-up section members [23, 47–49], coupled all DOFs of the nodes located at the centres of
258 the actual screws on the component channel section members. The 'Fasteners' approach
259 proposed by Phan et al. [50] employed mesh-independent fastener elements [37] to model the
260 actual screws, where the properties of the screws were obtained from the backbone curves
261 generated by Phan and Rasmussen [51]. The numerical failure modes and axial load–end

shortening curves of a typical specimen – I-90×70* – obtained using the three described interconnection approaches are shown in Figs. 12 and 13, respectively, indicating that the 'Actual screws' and 'Fasteners' approaches are in good agreement with the experimental results. Considering the higher computational efficiency, the 'Fasteners' approach was selected to simulate the interconnections in the built-up I-section stub columns studied herein.

3.2.3. Imperfections and loads

With regard to the incorporation of initial local geometric imperfections into each stub column FE model, an elastic eigenvalue buckling analysis [37] was adopted to obtain the corresponding lowest local buckling mode [52–55], which was determined as the pattern of initial local geometric imperfections and then input into the nonlinear analysis. To assess the sensitivity to the initial local geometric imperfections, four local geometric imperfection magnitudes, including the measured magnitude ω_l and three generalised magnitudes – 0.05t, 0.1t and 0.15t, were utilised to scale the distribution pattern. Static analyses [37] were conducted to obtain the local buckling behaviour and cross-sectional resistances of the S700 high-strength CFS built-up I-section stub column FE models. Artificial damping, with a dissipated energy coefficient of 0.0002 and a stabilization ratio of 0.05, was applied to overcome the convergence issues in some models.

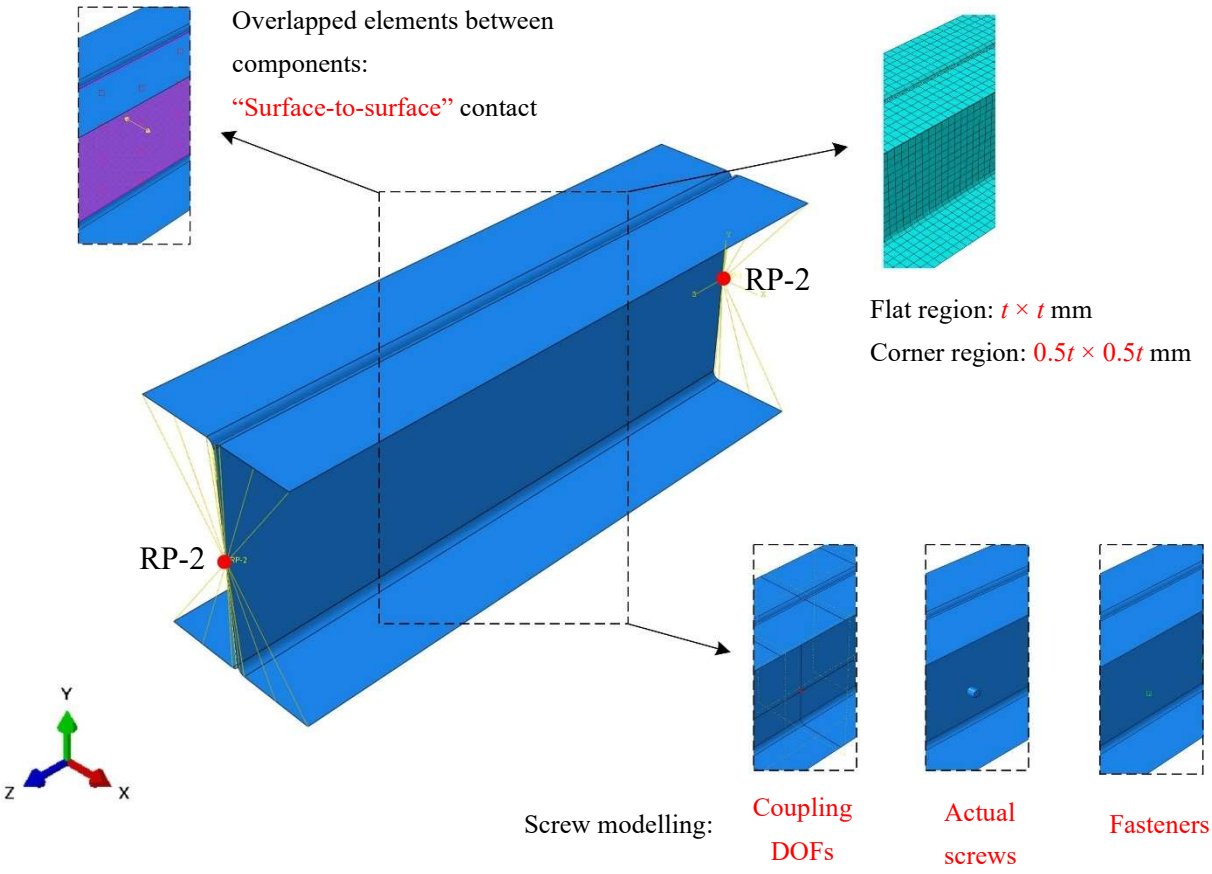
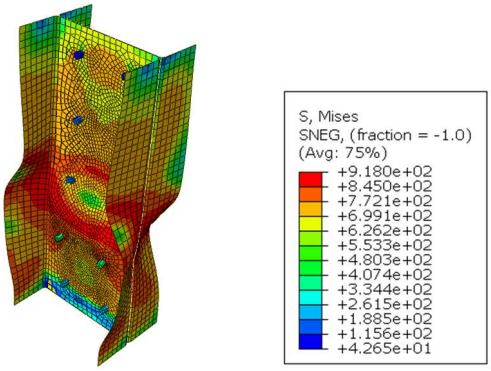


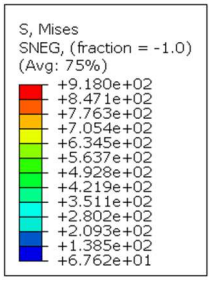
Fig. 11. FE model of CFS built-up I-section stub column.



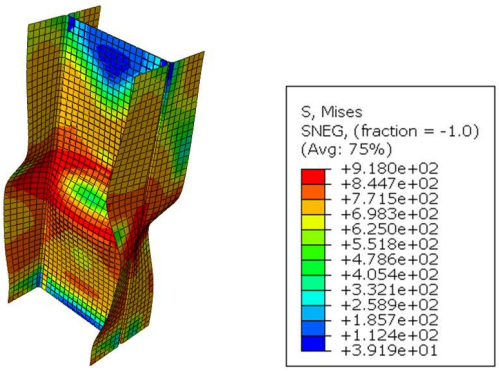
(a) Test – 546.5 kN



(b) FE with 'Actual screws' – 544.7 kN



(c) FE with 'Coupling DOFs' – 580.0 kN



(d) FE with 'Fasteners' – 551.0 kN

Fig. 12. Comparison of test and numerical failure modes of specimen I-90×70* with different interconnection approaches.

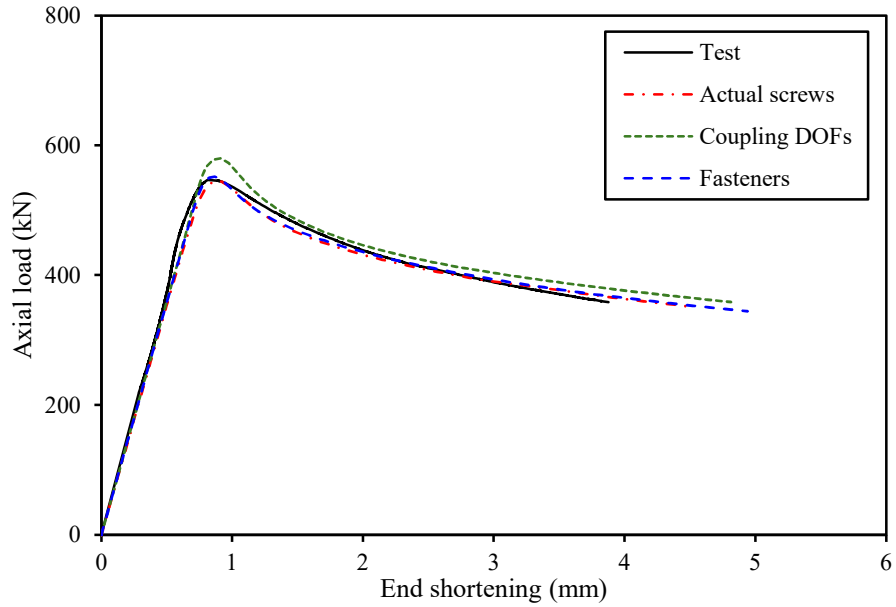
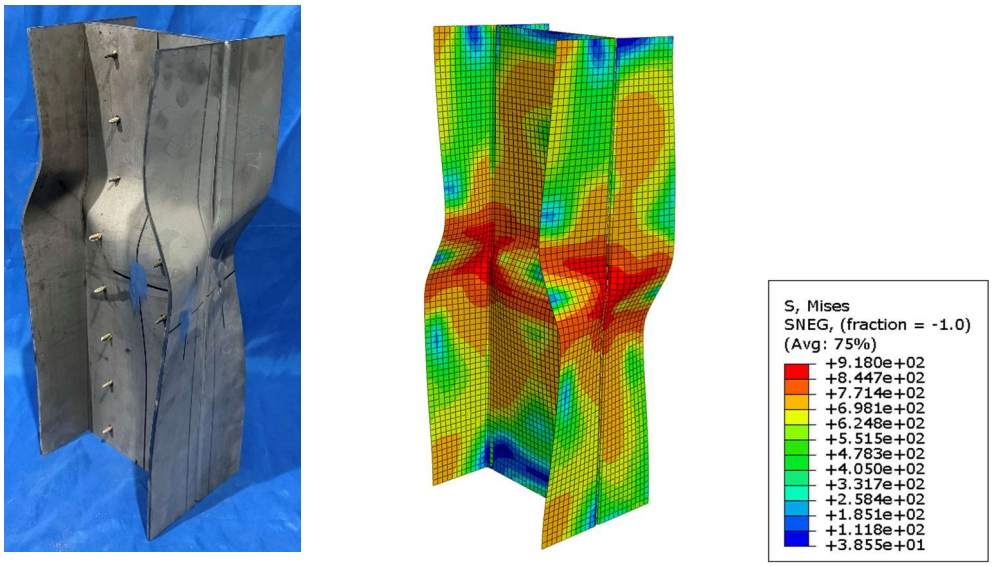


Fig. 13. Test and numerical axial load–end shortening curves of specimen I-90×70* with different interconnection approaches.

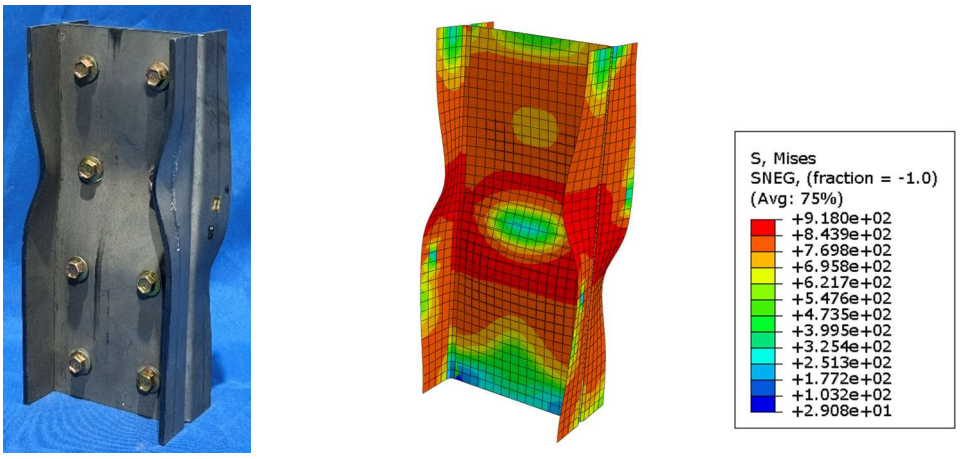
3.2.4. Validation of FE models

The developed stub column FE models were validated with reference to the experimental failure loads and modes and axial load–end shortening curves. Table 6 reports the mean ratios of the ultimate loads obtained from the FE analyses to the test failure loads for all stub column specimens and the corresponding coefficients of variation (COVs), showing that (i) all four imperfection magnitudes result in accurate and consistent failure load predictions and (ii) the measured imperfection magnitudes and the generalised imperfection magnitude of 0.1t result in the most accurate failure load predictions. The experimental and numerical failure modes of two typical stub column specimens, I-140×120 and I-80×50, are shown in Fig. 14, indicating good agreement. The axial load–end shortening curves obtained from the tests are also well

captured by numerical modelling, as shown in Fig. 15. In conclusion, the developed FE models have been shown to be capable of accurately simulating the experimental behaviour of S700 high-strength CFS built-up I-section stub columns.



(a) I-140×120



(b) I-80×50

Fig. 14. Comparison of test and numerical modes for typical S700 high-strength built-up I-section stub column specimens.

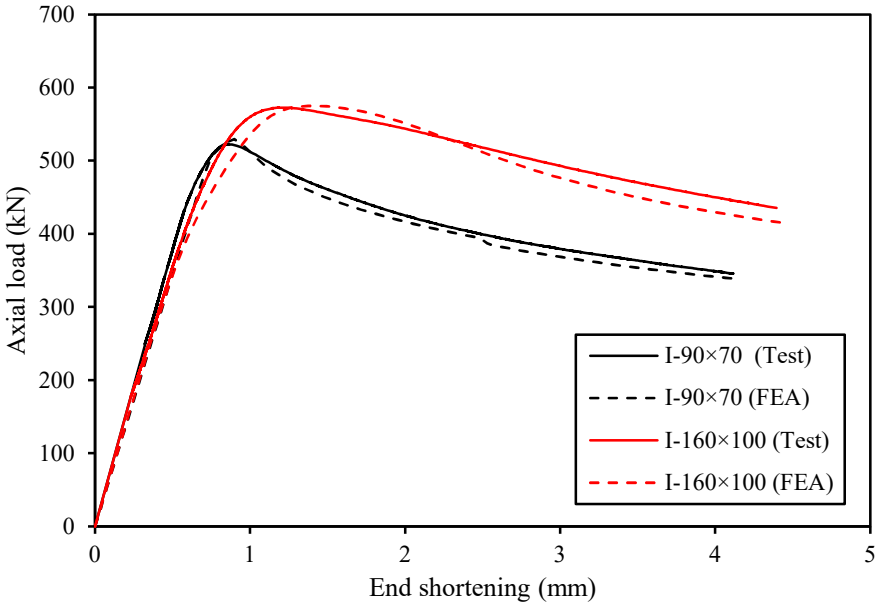


Fig. 15. Comparison of test and numerical axial load–end shortening curves for typical S700 high-strength built-up I-section stub column specimens.

Table 6

Comparisons of test failure loads with numerical failure loads for various initial local geometric imperfection magnitudes.

Specimen ID	FE P_u/Test P_u			
	ω_l	0.05t	0.1t	0.15t
I-60×40	1.09	1.11	1.11	1.05
I-80×50	1.03	1.04	1.04	1.00
I-90×70	1.00	1.02	1.00	0.96
I-90×70*	0.98	1.00	0.98	0.94
I-100×100	1.01	1.00	1.00	0.99
I-100×100*	1.00	1.00	1.00	0.99
I-120×90	1.00	1.02	1.00	0.99
I-120×90*	0.99	1.02	0.99	0.98
I-140×120	0.99	1.11	0.99	0.98
I-140×120*	1.00	1.02	1.00	1.00
I-160×100	0.97	1.00	0.97	0.96
I-160×100*	1.01	1.01	1.00	0.99
Mean	1.01	1.03	1.01	0.99
COV	0.03	0.04	0.04	0.04

4. Parametric studies

The validated FE models were used to conduct parametric studies to generate further numerical data over a wide range of cross-sectional dimensions. Table 7 lists the geometric dimensions of the component channel sections simulated in the parametric studies. Following the numerical modelling approach established in Section 3.2 and the initial local geometric imperfection magnitude of 0.1t, a total of 200 FE models were created. In order to include both slender and non-slender component channel sections, the outer cross-sectional heights h were varied between 70 mm and 200 mm, while the outer cross-sectional widths b were varied between 40 mm and 150 mm, with the thicknesses t ranging from 2.0 mm to 5.0 mm. For all stub column FE models, the member lengths were set equal to three times the average of nominal outer heights and widths of the component channel sections. Regarding the screw arrangements, screws located at the quarter-heights of the built-up I-sections were employed in the parametric studies. Note that the effect of screw spacing on load-carrying capacities of built-up section stub columns is insignificant [40, 50, 56], the evenly distributed screw spacing was thus taken equal to 50 mm. In contrast, the dimensions of geometric parameters, including cross-sectional height h, cross-sectional width b and thickness t, influenced the cross-sectional area and thus significantly affected the resistances of built-up section stub columns.

Table 7

Geometric dimensions of S700 high-strength CFS built-up I-section stub column FE models selected for parametric studies.

Section ID	a (mm)	s (mm)	h (mm)	b (mm)	t (mm)
I-70×40		7.5	70	40	2.0–4.0
I-80×60		5	80	60	2.0–4.0
I-80×70		12.5	80	70	2.0–4.0
I-100×70		27.5	100	70	2.0–4.0
I-100×80		10	100	80	2.0–5.0
I-100×90		17.5	100	90	2.0–5.0
I-130×110		5	130	110	2.0–4.0
I-140×100		5	140	100	2.0–4.0
I-140×110		12.5	140	110	2.0–4.0
I-140×120	50	20	140	120	2.0–4.0
I-150×100		12.5	150	100	2.0–4.0
I-170×100		27.5	170	100	2.0–4.0
I-180×150		22.5	180	150	2.0–4.0
I-190×100		17.5	190	100	2.0–4.0
I-190×110		25	190	110	2.0–4.0
I-190×150		5	190	150	2.0–4.0
I-200×100		25	200	100	2.0–4.0
I-200×120		15	200	120	2.0–4.0
I-200×150		12.5	200	150	2.0–4.0

5. Current design guidelines

5.1. General

The applicability of the Effective Width Method (EWM), as specified in EN 1993-1-3 [30] and AISI S100 [31], and the Direct Strength Method (DSM), as specified in AISI S100 [31], to the studied S700 CFS built-up I-sections was assessed by comparing the test and numerical failure loads P_u with the unfactored failure load predictions P_{pred}. A modified DSM is also proposed.

5.2. Effective Width Method (EWM)

5.2.1. Slenderness limits for cross-sectional classification

For the EWM specified in EN 1993-1-3 (EC3) [30] and AISI S100 (AISI) [31], the built-up I-sections are treated as the sum of two component channel sections, as shown in Fig. 16. The component channel sections were firstly classified according to the prescribed local slenderness limits; the compression resistances were then calculated. There are effectively 2 classes in compression in EN 1993-1-3 [30] and AISI S100 [31], i.e. Class 1–3 (non-slender) and Class 4 (slender) cross-sections. Regarding Class 1–3 and non-slender cross-sections, local buckling occurs after the material yield load is reached. In contrast, local buckling occurs prior to reaching the material yield load for Class 4 and slender cross-sections. The flat width-to-thickness ratio c/t of the most slender constituent plate element was compared to the corresponding slenderness limit to classify the component channel sections. The flat width is denoted as c_w for the width of the internal webs and c_f for the width of the outstand flanges, as displayed in Fig. 16. Table 8 reports the codified slenderness limits for the internal and outstand plate elements in compression, where $\varepsilon_{EC3} = \sqrt{235 / f_y}$ and $\varepsilon_{AISI} = \sqrt{E / f_y}$ are the material coefficients. Figs. 17 and 18 present the graphical assessment results of the applicability of the existing codified slenderness limits for internal and outstand plate elements in compression, respectively, where the test and numerical failure loads P_u are normalised by the yield loads P_y and plotted against the ratios of $c/(t\varepsilon_{EC3})$ and $c/(t\varepsilon_{AISI})$. It can be seen from Figs. 17 and 18 that

both codified slenderness limits for internal webs and outstand flanges are suitable for S700 high-strength CFS built-up I-section stub columns.

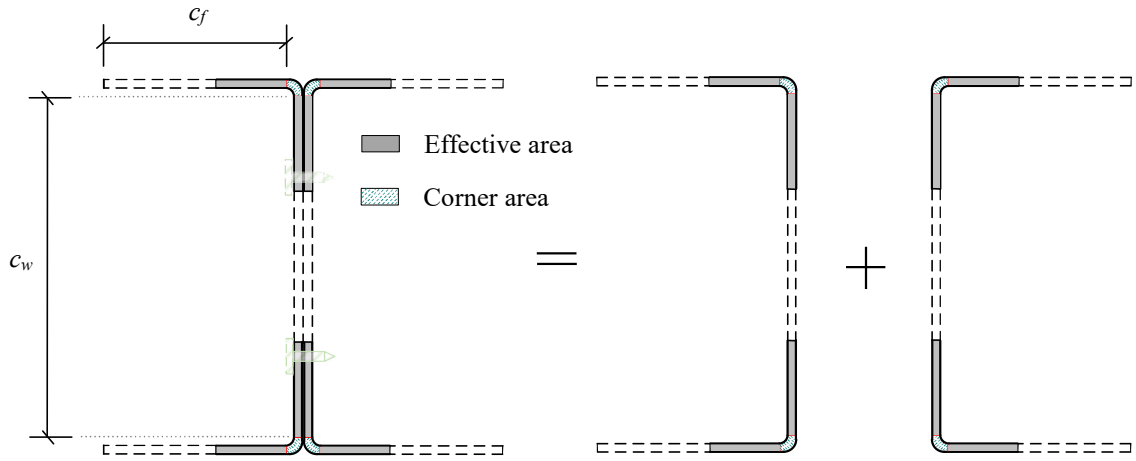
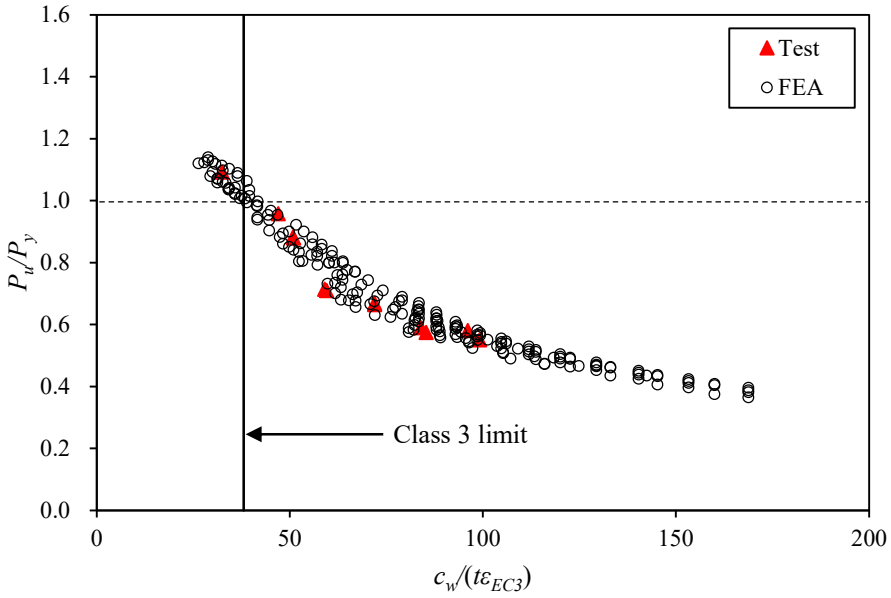


Fig. 16. Design treatment and flat width definition in EWM.

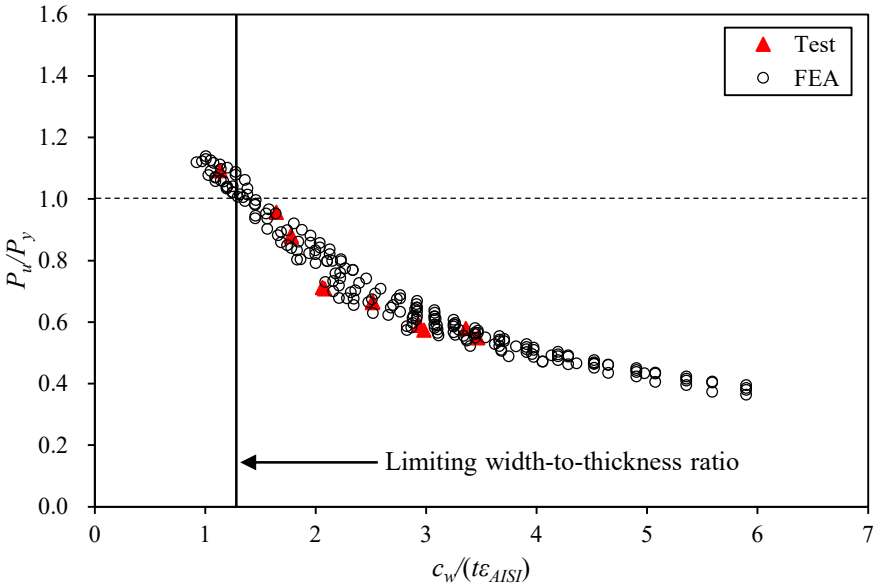
Table 8

Summary of codified slenderness limits between slender and non-slender plate elements in compression.

Design code	Internal element	Outstand element
EN 1993-1-3	$38\varepsilon_{EC3}$	$14\varepsilon_{EC3}$
AISI S100	$1.28\varepsilon_{AISI}$	$0.42\varepsilon_{AISI}$

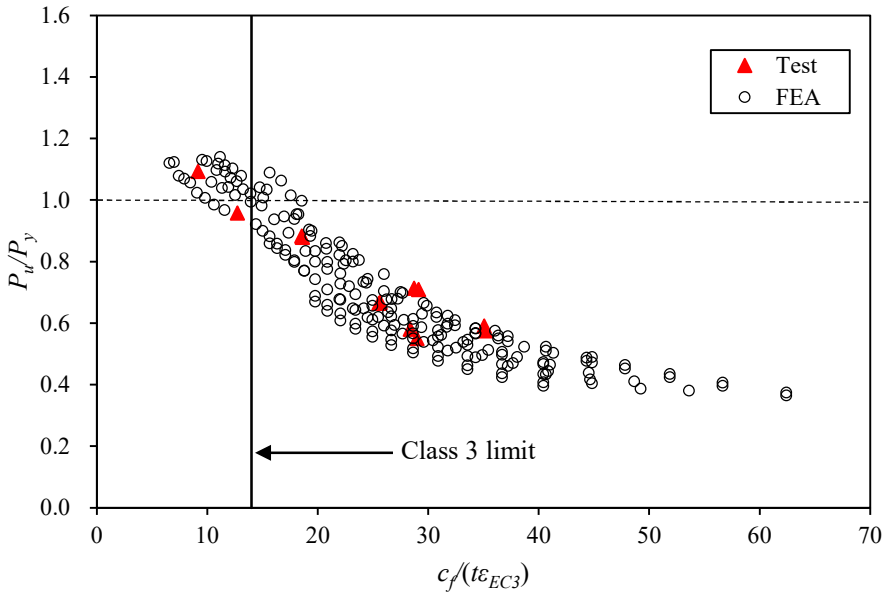


(a) EN 1993-1-3

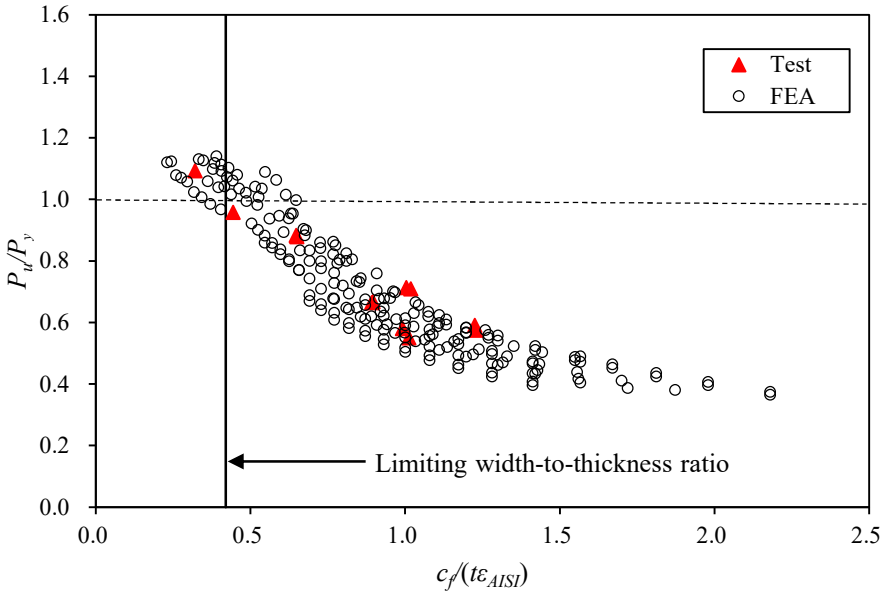


(b) AISI S100

Fig. 17. Assessment of slenderness limits for internal webs in compression.



(a) EN 1993-1-3



(b) AISI S100

Fig. 18. Assessment of slenderness limits for outstand flanges in compression.

5.2.2. Cross-sectional compression resistance

The cross-sectional compression resistance is specified in both design codes as the effective

401 resistance $A_{eff}f_y$ for Class 4 (slender) cross-sections and the yield load Af_y for Class 1–3 (non-
402 slender) cross-sections, where A_{eff} is the effective cross-sectional area and A is the gross cross-
403 sectional area. For a slender cross-section, the effective area A_{eff} is equal to the sum of the
404 effective areas of all plate elements and the full areas of the corners. The effective area of each
405 slender plate element is determined by multiplying the effective plate element width c_{eff} by the
406 plate thickness t. The EC3 and AISI effective widths – $c_{eff,EC3}$ and $c_{eff,AISI}$, are given by Eqs. (4)
407 and (5), respectively, where ψ is the stress distribution factor and equal to 1.0 for plate elements
408 under pure compression and λ_p is the slenderness of the plate element and calculated using Eq.
409 (6), where k is the buckling factor and equal to 4.0 and 0.43 for internal webs and outstand
410 flanges, respectively.

411
$$c_{eff,EC3} = \begin{cases} c\left(\dfrac{1}{\lambda_p} - \dfrac{0.188}{\lambda_p^2}\right) \le c & \text{for outstand plate elements} \\ c\left(\dfrac{1}{\lambda_p} - \dfrac{0.055(3+\psi)}{\lambda_p^2}\right) \le c & \text{for internal plate elements} \end{cases} \quad (4)$$

412
$$c_{eff,AISI} = c\left(\frac{1}{\lambda_p} - \frac{0.22}{\lambda_p^2}\right) \le c \quad (5)$$

413
$$\lambda_p = \begin{cases} \dfrac{c/t}{28.4\varepsilon_{EC3}\sqrt{k}} & \text{EN 1993-1-3} \\ 1.052\dfrac{c/t}{\varepsilon_{AISI}\sqrt{k}} & \text{AISI S100} \end{cases} \quad (6)$$

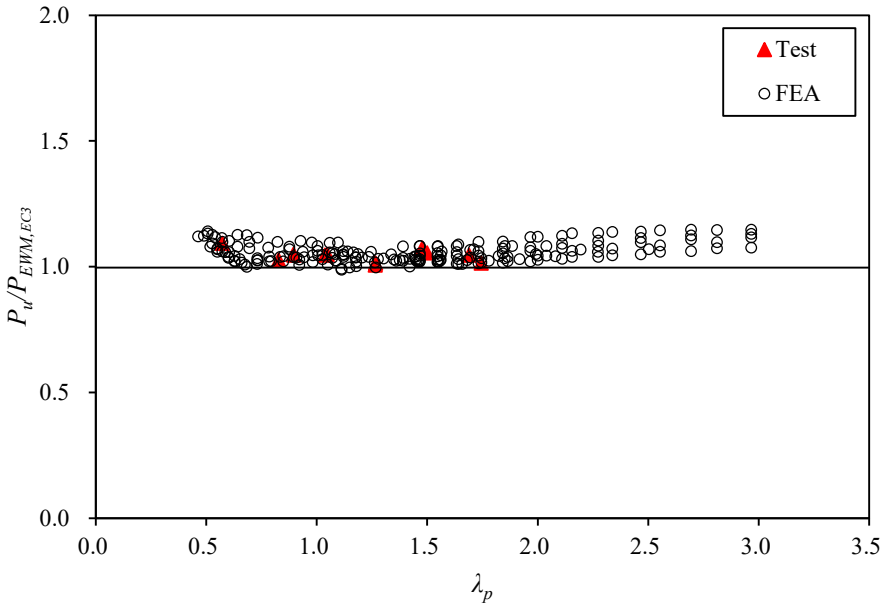
414 The applicability of the EC3 and AISI EWM to S700 high-strength CFS built-up I-section stub
415 columns was assessed by comparing the predicted failure loads with those obtained from the
416 tests and FE simulations. Table 9 reports the mean test and numerical to EWM predicted failure
417 load ratios, with $P_u/P_{EWM,EC3}$ and $P_u/P_{EWM,AISI}$ equal to 1.06 and 1.10 and the corresponding

COVs of 0.04 and 0.04, respectively, while Figs. 19(a) and 19(b) respectively display the ratios of $P_u/P_{EWM,EC3}$ and $P_u/P_{EWM,AISI}$ plotted against λ_p of the webs of the component channel sections. It can be concluded that (i) the codified EWM in EN 1993-1-3 [30] and AISI S100 [31] provided accurate and consistent failure load predictions for S700 high-strength CFS built-up I-section stub columns, and (ii) the AISI predicted failure loads were slightly more conservative compared with their EC3 counterparts.

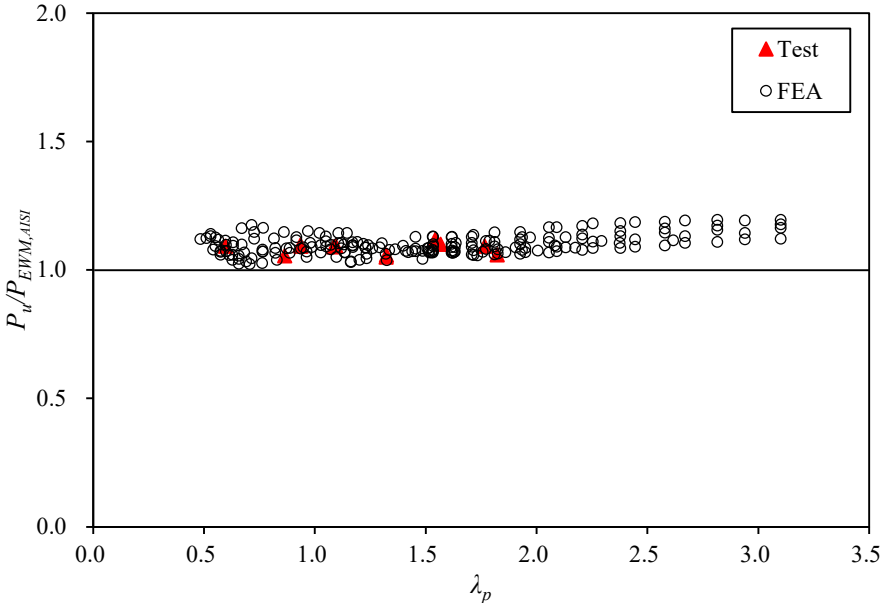
Table 9

Comparisons of experimental and numerical failure loads with predicted failure loads for S700 high-strength built-up I-section stub columns.

	No. of test data	No. of FE data	Mean	COV
$P_u/P_{EWM,EC3}$	12	200	1.06	0.04
$P_u/P_{EWM,AISI}$			1.10	0.04
P_u/P_{DSM}			1.02	0.03
$P_u/P_{DSM,\,pro}$			1.06	0.02



(a) EN 1993-1-3



(b) AISI S100

Fig. 19. Comparison of experimental and numerical failure loads with predicted failure loads from EWM.

5.3. Direct Strength Method (DSM)

Unlike the EWM, which relates the cross-sectional compression resistance to the slenderness of the individual plate elements and can become cumbersome for the design of cross-sections with complex geometries, the DSM resistance P_{DSM} is calculated based on the full cross-sectional slenderness λ_l, as given in Eq. (7), where $\lambda_l = \sqrt{P_y / P_{crl}}$ and P_{crl} is the elastic critical local buckling load of the built-up I-section determined using the finite strip software CUFSM [57]. The measured dimensions and material properties were used to model the built-up I-sections in CUFSM [57], while the screws were modelled as solid blocks, as successfully adopted in previous finite strip analyses of CFS built-up section members [17–19]. An elastic buckling analysis was conducted to obtain the signature curve, from which the lowest point was taken as the elastic local buckling load. The signature curve of a typical built-up I-section

column specimen – specimen I-120×90 – is shown in Fig. 20. A similar full cross-sectional slenderness-based design approach is also employed in the continuous strength method [58–60]. Note that the effect of shear deformations of the screws at the interface between the cold-formed sections was not considered herein in the determination of the elastic buckling loads, since the demands on the screws are low in the studied configuration (featuring local rather than global buckling) and no screw failures were observed [2, 61–63].

$$P_{DSM} = \begin{cases} P_y & \text{for } \lambda_l \le 0.776 \\ P_y \left[1 - 0.15 \left(\frac{1}{\lambda_l} \right)^{0.8} \right] \left(\frac{1}{\lambda_l} \right)^{0.8} & \text{for } \lambda_l > 0.776 \end{cases} \quad (7)$$

The DSM is included in AISI S100 [31] and its applicability to the design of S700 high-strength CFS built-up I-section stub columns was evaluated herein. As reported in Table 9, the mean ratio of P_u/P_{DSM} is 1.02 and the corresponding COV is 0.03. Fig. 21 displays the comparisons graphically, where the ratios of P_u/P_{DSM} are plotted against the local buckling slenderness λ_l. Both the quantitative and graphical assessment results indicate that the DSM yielded more accurate and consistent failure load predictions for S700 high-strength CFS built-up I-section stub columns than the codified EWM [30, 31], but with some points on the unsafe side.

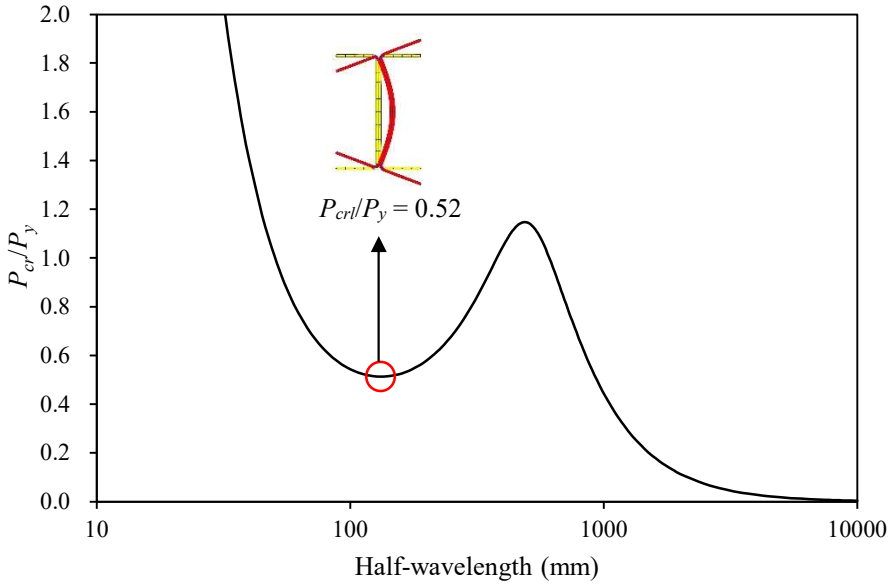


Fig. 20. Signature curve of typical built-up stub column I-120×90.

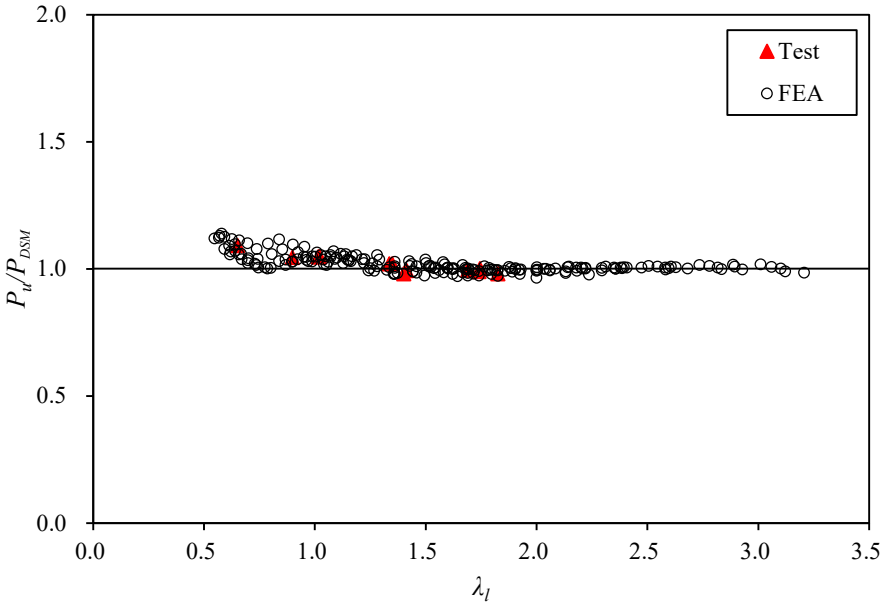


Fig. 21. Comparison of test and numerical failure loads with predicted failure loads from DSM.

6. Modified Direct Strength Method

The current semi-empirical DSM formulae were developed based on the data bank of CFS single section members, and the relevant coefficients should be revised for high-strength CFS built-up I-section members. Reviewing the assessment results of the codified DSM, a modified

475 DSM is proposed for predicting the local buckling resistances of S700 high-strength CFS built-
476 up I-section stub columns. The new design equation follows the same format of the codified
477 DSM but adopts new coefficients obtained from curve-fitting, as given in Eq. (8). Fig. 22 plots
478 the test and numerical failure loads P_u against the cross-sectional slenderness λ_l, along with the
479 codified and modified DSM strength curves, indicating the improved design accuracy of the
480 modified DSM strength curve. The accuracy of the proposed modified DSM approach was
481 evaluated based on the test and FE results. The graphical assessment results are shown in Fig.
482 23 and the quantitative assessment results are shown in Table 9, where the mean ratio of
483 $P_u/P_{DSM,prop}$ is equal to 1.06, with the corresponding COV of 0.02, revealing that the modified
484 DSM results in accurate, consistent and safe-side predicted failure loads for S700 high-strength
485 CFS built-up I-section stub columns.

486
$$P_{DSM,prop} = \begin{cases} P_y \ (0.15+0.68^{\lambda_l^{2.61}}) & \text{for } \lambda_l \le 0.787 \\ P_y \left[0.97 - 0.15 \left(\frac{1}{\lambda_l} \right)^{0.85} \right] \left(\frac{1}{\lambda_l} \right)^{0.85} & \text{for } \lambda_l > 0.787 \end{cases} \quad (8)$$

487

488

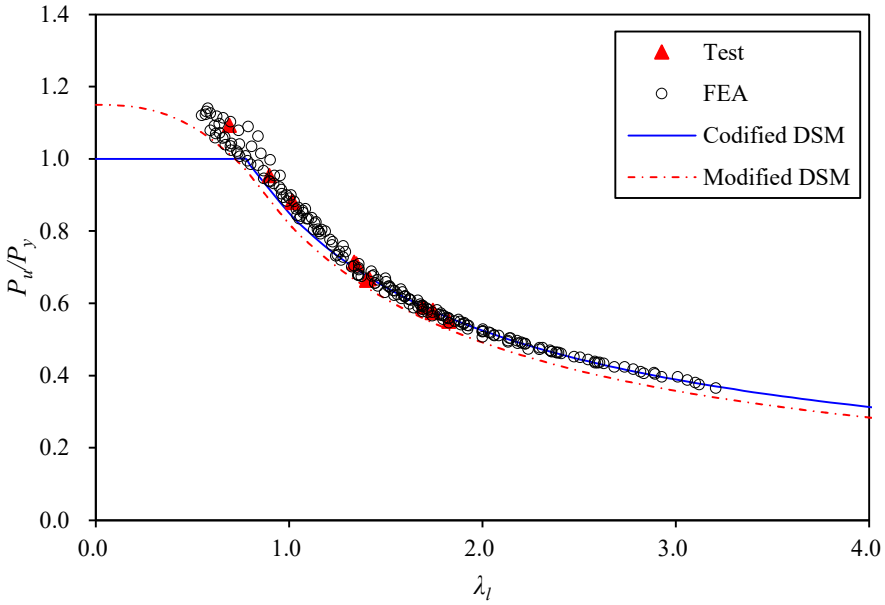


Fig. 22. Comparison of test and numerical results with codified and modified DSM curves.

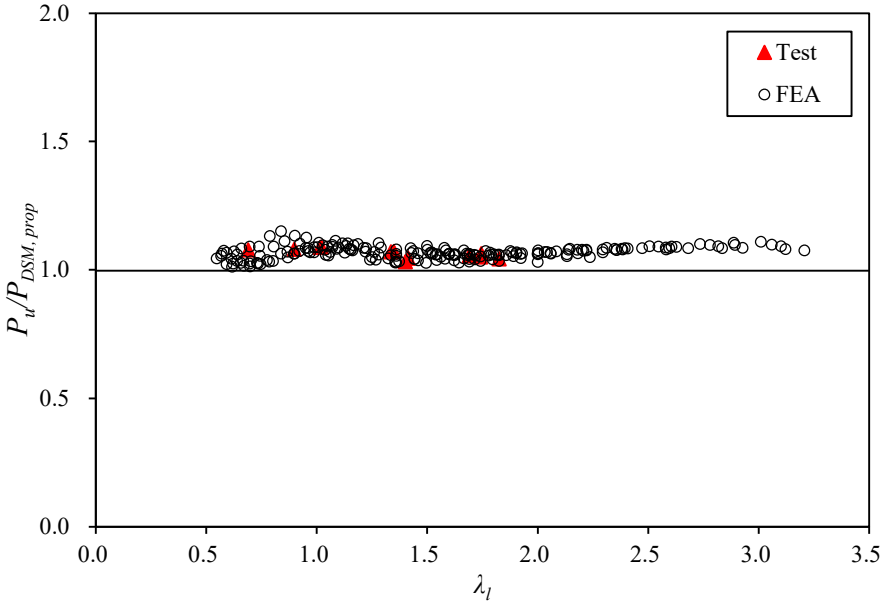


Fig. 23. Comparison of test and numerical failure loads with predicted failure loads from modified DSM.

7. Reliability analysis

Based on the statistical analysis procedures in AISI S100 [31], the reliability of the proposed modified DSM for S700 high-strength CFS built-up I-section stub columns was evaluated. The

key calculated statistical parameters are presented in Table 10, where P_m and V_p are the mean ratio and COV of $P_u/P_{DSM,prop}$, respectively, ϕ_c is the resistance factor and equal to 0.85 [31] and β is the reliability index. The reliability index β is calculated from Eq. (9), where C_p is a correction factor relating to the number of data points and equal to 1.01, F_m and M_m are the mean values of the fabrication factor and material factors and taken equal to 1.00 and 1.10 [19], respectively, and V_F and V_M are the COVs of the fabrication factor and the material factor and equal to 0.05 and 0.10, respectively [50]. Regarding the design of CFS structures, the typical ratio of dead load (DD) to live load (LD) is taken equal to 1/5 and thus the computed value of V_Q is 0.207 [50]. For the critical load combination of 1.2DD + 1.6LD, the calibration coefficient C_ϕ is equal to 1.521 for structural design [31]. The calculated reliability index β, as reported in Table 10, is greater than the target value of 2.5 in AISI S100 [31], indicating the reliability of the proposed modified DSM for S700 high-strength CFS built-up I-section stub columns.

$$\beta = \frac{\ln\left(\frac{C_\phi M_m F_m P_m}{\phi_c}\right)}{\sqrt{V_M^2 + V_F^2 + C_P V_P^2 + V_Q^2}} \tag{9}$$

Table 10

Reliability analysis results for proposed modified DSM.

Number of data points	P_m (Mean)	V_p (COV)	ϕ_c	β
212	1.06	0.02	0.85	3.13

519 **8. Conclusions**

520

521 Testing and numerical modelling have been carried out to investigate the cross-sectional
522 buckling behaviour and resistance of S700 high-strength cold-formed steel (CFS) built-up I-
523 section stub columns. The testing programme included tensile coupon tests, initial local
524 geometric imperfection measurements and twelve stub column tests. The obtained test results,
525 including the axial load–end shortening curves, failure loads and failure modes have been
526 described. A numerical programme was then conducted, where FE models were established and
527 validated against the test results, and parametric studies were conducted to generate further
528 numerical data over a wide range of cross-sectional dimensions. On the basis of the
529 experimental and numerical data, the applicability of the effective width method (EWM), as set
530 out in EN 1993-1-3 [30] and AISI S100 [31], and the direct strength method (DSM), as set out
531 in AISI S100 [31], to S700 high-strength CFS built-up I-section stub columns was evaluated.
532 The evaluation results indicated that (i) both the codified EWM and DSM resulted in accurate
533 and consistent cross-sectional resistance predictions in general, (ii) the codified DSM yielded a
534 higher level of design accuracy and consistency than the codified EWM, but with many failure
535 load predictions on the unconservative side. Finally, a modified DSM strength curve was
536 proposed and shown to provide accurate, consistent and safe-sided failure load predictions for
537 S700 high-strength CFS built-up I-section stub columns. Building on the current research into
538 the cross-sectional resistance of S700 high-strength CFS built-up I-section stub columns, the
539 behaviour of S700 high-strength CFS built-up I-section columns and beam–columns, with due

allowance for the effect of shear deformations on the member stability, will be studied in future research. In addition, it is necessary to evaluate the applicability of the modified DSM for CFS built-up I-section members with the nominal yield strengths exceeding 700 MPa.

Acknowledgements

The research carried out and described in this paper was supported by the National Natural Science Foundation of China (No. 52308163).

References

[1] D. Phan, K. Rasmussen, Flexural rigidity of cold-formed steel built-up members, Thin-Walled Structures 140 (2019) 438–449.

[2] K. Rasmussen, M. Khezri, B. Schafer, H. Zhang, The mechanics of built-up cold-formed steel members, Thin-Walled Structures 154 (2020) 106756.

[3] H. Li, C. Jin, Q. Li, B. Young, Experimental investigation of cold-formed stainless steel built-up closed section stub columns, Engineering Structures 306 (2024) 117657.

[4] A. Su, H. Yang, Y. Wang, Y. Wang, Experimental and numerical investigations of S960 hot-rolled ultra-high strength steel seamless circular hollow section beam–columns, Thin-Walled Structures 200 (2024) 111909.

[5] A. Su, Y. Wang, Y. Wang, K. Rasmussen, L. Gardner, Behaviour and design of S960 ultra-

high strength steel non-slender welded I-section beam–columns, Engineering Structures 304 (2024) 117602.

[6] A. Su, J. Cheng, X. Li, Y. Zhong, S. Li, O. Zhao, K. Jiang, Unified machine-learning-based design method for normal and high strength steel I-section beam–columns, Thin-Walled Structures 199 (2024) 111835.

[7] A. Su, Y. Wang, K. Rasmussen, L. Gardner, Structural performance and design of S960 ultra-high strength steel non-slender welded I-sections subjected to combined loading, Engineering Structures 293 (2023) 116593.

[8] A. Su, O. Zhao, Experimental and numerical investigations of S960 ultra-high strength steel slender welded I-section columns failing by local–flexural interactive buckling, Thin-Walled Structures 180 (2022) 109898.

[9] A. Su, Y. Sun, Y. Liang, O. Zhao, Membrane residual stresses and local buckling of S960 ultra-high strength steel welded I-section stub columns, Thin-Walled Structures 161 (2021) 107497.

[10] A. Su, K. Jiang, M. Wang, O. Zhao, S960 ultra-high strength steel slender welded I-section beam–columns: Testing, numerical modelling and design, Thin-Walled Structures 177 (2022) 109452.

[11] Y. Sun, Y. Liang, A. Su, O. Zhao, Local–flexural interactive buckling of S690 high strength steel slender welded I-section columns: Testing, modelling and design, Thin-Walled Structures 166 (2021) 108064.

[12] Y. Sun, Y. Liang, O. Zhao, B. Young, Experimental and numerical investigations of S690

high-strength steel welded I-sections under combined compression and bending, Journal of Structural Engineering 147(5) (2021) 04021054.

[13] G. Shi, K. Xu, H. Ban, C. Lin, Local buckling behaviour of welded stub columns with normal and high strength steels, Journal of Constructional Steel Research 119 (2016) 144–153.

[14] G. Shi, W. Zhou, C. Lin, Experimental investigation on the local buckling behaviour of 960 MPa high strength steel welded section stub columns, Advances in Structural Engineering 18(3) (2015) 423–437.

[15] X. Yun, Y. Zhu, X. Meng, L. Gardner, Welded steel I-section columns: Residual stresses, testing, simulation and design, Engineering Structures 282 (2023) 115631.

[16] M. Abbasi, K. Rasmussen, M. Khezri, B. Schafer, Experimental investigation of the sectional buckling of built-up cold-formed steel columns, Journal of Constructional Steel Research 203 (2023) 107803.

[17] J. Zhang, B. Young, Numerical investigation and design of cold-formed steel built-up open section columns with longitudinal stiffeners, Thin-Walled Structures 89 (2015) 178–191.

[18] J. Zhang, B. Young, Compression tests of cold-formed steel I-shaped open sections with edge and web stiffeners, Thin-Walled Structures 52 (2012) 1–11.

[19] Q. Li, B. Young, Experimental and numerical investigation on cold-formed steel built-up section pin-ended columns, Thin-Walled Structures 170 (2022) 108444.

[20] K. Roy, T. Ting, H. Lau, J. Lim, Nonlinear behaviour of back-to-back gapped built-up cold-formed steel channel sections under compression, Journal of Constructional Steel Research

603 147 (2018) 257–276.
604 [21] K. Roy, T. Ting, H. Lau, J. Lim, Nonlinear behaviour of axially loaded back-to-back built-
605 up cold-formed steel un-lipped channel sections, Steel Composite Structures 28(2) (2018)
606 233–250.
607 [22] K. Roy, T. Ting, H. Lau, J. Lim, Effect of thickness on the behaviour of axially loaded
608 back-to-back cold-formed steel built-up channel sections-Experimental and numerical
609 investigation, Structures 16 (2018) 327–346.
610 [23] Y. Li, Y. Li, S. Wang, Z. Shen, Ultimate load-carrying capacity of cold-formed thin-walled
611 columns with built-up box and I section under axial compression, Thin-Walled Structures
612 79 (2014) 202–217.
613 [24] T. Ting, K. Roy, H. Lau, J. Lim, Effect of screw spacing on behaviour of axially loaded
614 back-to-back cold-formed steel built-up channel sections, Advances in Structural
615 Engineering 21(3) (2018) 474–487.
616 [25] L. Wang, B. Young, Behaviour of cold-formed steel built-up sections with intermediate
617 stiffeners under bending. I: Tests and numerical validation, Journal of Structural
618 Engineering 142(3) (2016) 04015150.
619 [26] L. Wang, B. Young, Behaviour of cold-formed steel built-up sections with intermediate
620 stiffeners under bending. II: Parametric study and design, Journal of Structural Engineering
621 142(3) (2016) 04015151.
622 [27] L. Wang, B. Young, Behaviour and design of cold-formed steel built-up section beams with
623 different screw arrangements, Thin-Walled Structures 131 (2018) 16–32.

624 [28] K. Roy, H. Lau, T. Ting, B. Chen, J. Lim, Flexural behaviour of back-to-back built-up cold-
625 formed steel channel beams: Experiments and finite element modelling, Structures 29
626 (2021) 235–253.
627 [29] K. Roy, H. Lau, T. Ting, B. Chen, J. Lim, Flexural capacity of gapped built-up cold-formed
628 steel channel sections including web stiffeners, Journal of Constructional Steel Research
629 172 (2020) 106154.
630 [30] EN 1993-1-3: 2024, Eurocode 3: Design of Steel Structures - Part 1-3: Supplementary
631 Rules for Cold-formed Members and Sheeting, European Committee for Standardization
632 (CEN), Brussels, 2024.
633 [31] AISI S100-16 (2022) w/S3-22, North American Specification for the Design of Cold-
634 Formed Steel Structural Members, American Iron and Steel Institute, Washington, DC,
635 2022.
636 [32] M. Huynh, C. Pham, G. Hancock, Design of screwed connections in cold-formed steels in
637 shear, Thin-Walled Structures 154 (2020) 106817.
638 [33] EN ISO 6892-1, Metallic Materials: Tensile Testing – Part 1: Method of Test at Room
639 Temperature, European Committee for Stanardization (CEN), Brussels, 2016.
640 [34] M. Kucukler, Z. Xing, L. Gardner, Behaviour and design of stainless steel I-section
641 columns in fire, Journal of Constructional Steel Research 165 (2020) 105890.
642 [35] H. Yuan, Y. Wang, L. Gardner, Y. Shi, Local–overall interactive buckling of welded
643 stainless steel box section compression members, Engineering Structures 67 (2014) 62–76.
644 [36] X. Meng, L. Gardner, Testing of hot-finished high strength steel SHS and RHS under

combined compression and bending, Thin-Walled Structures 148 (2020) 106262.

[37] ABAQUS, ABAQUS/Standard User's Manual Volumes I-III and ABAQUS CAE Manual, Version 2018, Hibbitt, Karlsson & Sorensen, Inc., Pawtucket, 2018.

[38] P. Kyvelou, L. Gardner, D. Nethercot, Finite element modelling of composite cold-formed steel flooring systems, Engineering Structures 158 (2018) 28–42.

[39] O. Zhao, B. Rossi, L. Gardner, B. Young, Experimental and numerical studies of ferritic stainless steel tubular cross sections under combined compression and bending, Journal of Structural Engineering 142(2) (2016) 04015110.

[40] K. Jiang, O. Zhao, Stainless steel built-up section stub columns: Testing, numerical modelling and design, Thin-Walled Structures 191 (2023) 111070.

[41] X. Meng, L. Gardner, Cross-sectional behaviour of cold-formed high strength steel circular hollow sections, Thin-Walled Structures 156 (2020) 106822.

[42] M. Theofanous, T. Chan, L. Gardner, Flexural behaviour of stainless steel oval hollow sections, Thin-Walled Structures 47(6-7) (2009) 776–787.

[43] Y. Wang, A. Su, H. Yang, J. Zhao, Y. Wang, S890 hot-rolled ultra-high strength steel (UHSS) seamless circular hollow section beam–columns: Testing, modelling and design, Thin-Walled Structures 197 (2024) 111583.

[44] B. Young, K. Rasmussen, Compression tests of fixed-ended and pin-ended cold-formed plain channels, Research Report-University of Sydney, School of Civil and Mining Engineering (1995).

[45] G. Li, Z. Wu, D. Wen, J. Shao, C. Hu, Experimental investigation on the cold-forming

effect of high strength cold-formed steel sections, Structures 58 (2023) 105615.

[46] M. Abbasi, K. Rasmussen, M. Khezri, B. Schafer, Computational modelling of built-up cold-formed steel columns and parametric studies, Thin-Walled Structures 191 (2023) 111035.

[47] Y. Cui, J. Zhang, C. Ma, M. Niu, K. Jiang, S. Li, A. Su, Testing, numerical modelling and design of G550 high strength cold-formed steel built-up section columns, Thin-Walled Structures (2023) 111529.

[48] X. Zhou, Y. Xiang, Y. Shi, L. Xu, Y. Zou, Simplified design method of cold-formed steel columns with built-up box sections, Engineering Structures 228 (2021) 111532.

[49] X. Liu, T. Zhou, Research on axial compression behaviour of cold-formed triple-lambs built-up open T-section columns, Journal of Constructional Steel Research 134 (2017) 102–113.

[50] D. Phan, K. Rasmussen, B. Schafer, Numerical investigation of the strength and design of cold-formed steel built-up columns, Journal of Constructional Steel Research 193 (2022) 107276.

[51] D. Phan, Strength and stiffness of built-up section columns abstract, University of Sydney, Sydney, Australia, 2020, PhD Thesis.

[52] M. Kucukler, L. Gardner, L. Macorini, Lateral–torsional buckling assessment of steel beams through a stiffness reduction method, Journal of Constructional Steel Research 109 (2015) 87-100.

[53] K. Roy, H. Lau, J. Lim, Effect of fastener spacing on axial strength of back-to-back built-

687 up cold-formed stainless steel un-lipped channels, Steel Compos Struct Int J (2018).
688 [54] Y. Dai, Z. Fang, K. Roy, G. Raftery, J.B. Lim, Optimal design of cold-formed steel face-
689 to-face built-up columns through deep belief network and genetic algorithm, Structures,
690 56 (2023) 104906.
691 [55] Y. Dai, K. Roy, Z. Fang, B. Chen, G. Raftery, J. Lim, Buckling resistance of axially loaded
692 cold-formed steel built-up stiffened box sections through experimental testing and finite
693 element analysis, Engineering Structures 302 (2024) 117379.
694 [56] D. Fratamico, S. Torabian, K. Rasmussen, B. Schafer, Experimental investigation of the
695 effect of screw fastener spacing on the local and distortional buckling behavior of built-up
696 cold-formed steel columns, in: CCFSS Proceedings of International Specialty Conference
697 on Cold-Formed Steel Structures (2016).
698 [57] B. Schafer, S. Adany, Buckling analysis of cold-formed steel members using CUFSM:
699 conventional and constrained finite strip methods, Proceedings of the 18th International
700 Specialty Conference on Cold-Formed Steel Structures, Orlando, Florida, USA, 2006.
701 [58] L. Gardner, X. Yun, F. Walport, The continuous strength method–review and outlook,
702 Engineering Structures 275 (2023) 114924.
703 [59] L. Gardner, X. Yun, A. Fieber, L. Macorini, Steel design by advanced analysis: material
704 modeling and strain limits, Engineering 5(2) (2019) 243–249.
705 [60] M. Bock, L. Gardner, E. Real, Material and local buckling response of ferritic stainless
706 steel sections, Thin-Walled Structures 89 (2015) 131–141.
707 [61] K. Roy, C. Mohammadjani, J. Lim, Experimental and numerical investigation into the

behaviour of face-to-face built-up cold-formed steel channel sections under compression, Thin-Walled Structures 134 (2019) 291–309.

[62] K. Roy, T. Ting, H. Lau, J. Lim, Experimental and numerical investigations on the axial capacity of cold-formed steel built-up box sections, Journal of Constructional Steel Research 160 (2019) 411–427.

[63] K. Roy, J. Lim, Numerical investigation into the buckling behaviour of face-to-face built-up cold-formed stainless steel channel sections under axial compression, Structures 20 (2019) 42–73.